International Journal of Pressure Vessels and Piping 180 (2020) 104025

Contents lists available at ScienceDirect

International Journal of Pressure Vessels and Piping

journal homepage: http://www.elsevier.com/locate/ijpvp

Out-of-plane constraint loss in three point bend specimens with notches

A.J. Horn [a,*], S. Cicero [b], D. Andrés [c,1]

[a] Wood Nuclear, 305 Bridgewater Place, Birchwood Park, Risley, Cheshire, WA3 6XG, UK
[b] LADICIM (Laboratory of Materials Science and Engineering), University of Cantabria, E.T.S. de Ingenieros de Caminos, Canales y Puertos, Av/ Los Castros 44, 39005, Santander, Cantabria, Spain
[c] Technology Department, UK Atomic Energy Authority, Culham Science Centre, Abingdon, Oxfordshire, OX14 3DB, UK

ARTICLE INFO

Keywords:
Blunt notch
Effective fracture toughness
Notch failure assessment diagram

ABSTRACT

This paper presents an experimental and numerical study of the effect of specimen thickness on the effective notch toughness K_{mat}^{ρ} for cleavage fracture measured using Single Edge Notch Bend (SENB) specimens containing a U-notch instead of a fatigue pre-crack. These specimens are typically used to measure a material's effective notch toughness K_{mat}^{ρ} and to assess failure of a structure containing a non-sharp defect using the Notch Failure Assessment Diagram (NFAD). Both the experimental data and the Finite Element (FE) failure predictions show a significant influence of specimen thickness on K_{mat}^{ρ}, over and above the microstructural weakest link effect arising from differences in the volume of the plastic zone. K_{mat}^{ρ} is a function of not only the in-plane effect of the notch radius, but also an out-of-plane constraint loss which itself is enhanced by the presence of the notch radius. Significant out-of-plane constraint loss occurred for notched specimens with a ratio of thickness B to width W of 0.5, a geometry that if pre-cracked would have met the minimum thickness requirement mandated by ASTM E1820. Doubling the thickness to $B/W = 1.0$ was sufficient to eliminate the out-of-plane constraint loss. The use of experimentally measured K_{mat}^{ρ} values in an NFAD assessment of a structure may therefore be non-conservative if $B/W<1.0$.

1. Introduction

The structural integrity of engineering structures is conventionally assessed using defect or flaw assessment procedures based on fracture mechanics approaches [e.g. [1–3]]. For a real or postulated defect, the crack driving force (e.g. the elastic-plastic energy release rate J or the elastic-plastic stress intensity factor K_J) under the loading conditions and temperature of interest is compared with the material fracture toughness. Such procedures assume flaws to be infinitely sharp. While this assumption may be appropriate for fatigue cracks, in other cases such as porosity, lack-of-fusion, corrosion damage, mechanical damage, or even design features such a crevices in tube-to-tubeplate assemblies, it can be an over-conservative assumption that can lead to a pessimistic assessment of the structure and a significant under-estimation of the safety margin against fracture.

Structural integrity assessments undertaken in accordance with [1–3] are carried out using a Failure Assessment Diagram (FAD) in which the ordinate K_r indicates the proximity to fracture. For primary loading only, K_r is defined as K_I/K_{mat}, where K_I is the linear elastic stress intensity factor and K_{mat} is the material toughness typically derived from fatigue pre-cracked fracture toughness specimens tested according to well-defined standards, e.g. Refs. [4–6]. The abscissa L_r indicates the proximity to failure by plastic collapse and is defined as P/P_L, where P is the applied load and P_L is the elastic-perfectly plastic limit load. K_r and L_r are both proportional to P and a linear loading line can be plotted on the FAD. When all inputs are best-estimate values, failure is predicted at its intersection with the failure assessment curve which is represented by $K_r = f(L_r)$ for $L_r<L_{r(max)}$ where $f(L_r)$ is the failure assessment curve, $L_{r(max)}$ is the ratio of the uniaxial flow stress $\overline{\sigma}$ to the uniaxial yield stress σ_y defined at 0.2% plastic strain, and $\overline{\sigma}$ is defined as the mean of σ_y and the ultimate tensile stress (UTS).

Over the last 25 years or so, several engineering assessment methodologies have been published in the literature for assessing structures that contain non-sharp defects using a modified form of the FAD called the Notch Failure Assessment Diagram (NFAD) [e.g. [7–12]]. The exact form of the NFAD varies from approach to approach. Taking the

* Corresponding author.
E-mail address: Anthony.Horn@woodplc.com (A.J. Horn).

[1] Address at the time of performing the work: LADICIM (Laboratory of Materials Science and Engineering), University of Cantabria, E.T.S. de Ingenieros de Caminos, Canales y Puertos, Av/Los Castros 44, 39005, Santander, Cantabria, Spain.

https://doi.org/10.1016/j.ijpvp.2019.104025
Received 2 April 2019; Received in revised form 26 November 2019; Accepted 30 November 2019
Available online 5 December 2019

Nomenclature

a	Crack or notch depth (from the notch mouth to the tip of the notch)
B	Specimen thickness
E	Elastic modulus
e_{max}	Strain at maximum load
$f(L_r)$	Failure assessment curve on the FAD
$f(L_r^\rho)$	Failure assessment curve on the NFAD
i	ith toughness value in a dataset (out of a total of N values)
J	Elastic-plastic energy release rate
J^ρ	J for a notch
J_{ESIS}	J obtained from load-displacement data using ESIS P2-92, Equation 7
K_I	Linear elastic stress intensity factor
K_I^ρ	Linear elastic stress intensity factor for a notch
K_J	J expressed in dimensions of K
K_J^ρ	J^ρ expressed in dimensions of K
K_{JC}^ρ	Critical value of K_J^ρ for an individual test specimen containing a notch
K_{mat}	K_{JC} measured using pre-cracked specimens at a defined P_f
K_{mat}^ρ	K_{JC} measured using notched specimens at a defined P_f
K_{min}	Minimum possible value of K_{mat}, defined as 20 MPa$\sqrt{\text{m}}$ in ASTM E1921
K_r	Fracture ratio, plotted on ordinate axis of the FAD
K_r^ρ	Fracture ratio for a notch, plotted on ordinate axis of the NFAD
L	Element size
L_r	Load ratio, plotted on the abscissa axis of the FAD
L_r^ρ	Load ratio for a notch, plotted on abscissa axis of the NFAD
$L_{r(max)}$	Maximum value of L_r defining vertical cut-off on the FAD
l	Material parameter describing sensitivity of K_{mat}^ρ / K_{mat} to σ_N/σ_y
m	Weibull modulus
n	Strain hardening exponent
N	Total number of toughness values in a dataset
r	Distance from the centre of curvature of the notch root radius
P	Applied load
P_f	Failure probability
P_L	Limit load
P_L^ρ	Limit load for a notch
R	Radius of boundary layer model
$R(m)$	Error function defined in Section 4.3.1
T	Temperature
T_0	Master Curve Reference Temperature
$u_1 u_2$	Displacements in the x_1 andx_2 directions respectively
V	Plastic zone
V_0	Reference volume taken as unity
W	Specimen width
$x_1 x_2 x_3$	Co-ordinate system
Y	Geometry factor used to define K_I
γ	Material parameter describing sensitivity of K_{mat}^ρ / K_{mat} to σ_N/σ_y
η	Proportionality constant to evaluate J from load vs. displacement
ν	Poisson's ratio
$\xi^{A,B}$	Estimate of the SSY scale factor
ρ	Notch root radius
θ	Angle subtended at the centre of curvature of the notch root radius
σ	Applied tensile stress
$\bar{\sigma}$	Flow stress, defined as the mean of σ_y and UTS
σ_1	Maximum principal stress
σ_N	Elastic notch tip opening stress
σ_0	Stress at the limit of proportionality
σ_w	Weibull stress
σ_u	Weibull parameter, defined as σ_w at $P_f = 0.632$
$\sigma_{w,min}$	Minimum value of Weibull stress in SSY corresponding to $K_{min} = 20$ MPa$\sqrt{\text{m}}$
σ_y	Yield stress defined at 0.2% plastic strain
CMOD	Crack Mouth Opening Displacement
CT	Compact Tension
FAD	Failure Assessment Diagram
FE	Finite Element
LLD	Load-Line Displacement
NFAD	Notch Failure Assessment Diagram
SSY	Small Scale Yielding
SSY^N	Small Scale Yielding for a notch
UTS	Ultimate Tensile Stress

approach described in Refs. [7,12] as an example, proximity to the two failure limits of plastic collapse and fracture is quantified by the parameters L_r^ρ and K_r^ρ. L_r^ρ is defined as P/P_L^ρ, where P_L^ρ is the elastic-perfectly plastic limit load for a component containing a notch of root radius ρ. K_r^ρ is defined as K_I^ρ / K_{mat}^ρ, where K_I^ρ is the linear-elastic notch stress intensity factor and K_{mat}^ρ is the effective notch toughness. The condition that the component does not fail is indicated by $K_r^\rho < f(L_r^\rho)$ for $L_r^\rho < L_{r(max)}$. Several authors [7,12–14] have shown that when the NFAD axes are defined by L_r^ρ and K_r^ρ instead of L_r and K_r, failure assessment curves are broadly independent of ρ. This enables the same failure assessment curve to be used in the NFAD as for the FAD.

Although the precise definitions of the parameters used in the various forms of NFAD vary between the different approaches, one similarity common to all NFAD approaches is the requirement to use an effective notch toughness K_{mat}^ρ in place of the material toughness K_{mat}, to calculate K_r^ρ. No testing standards are currently available to provide guidance on how K_{mat}^ρ can be measured using fracture toughness specimens that contain notches instead of pre-cracks. In the absence of dedicated test standards for notched specimens, test standards originally designed for pre-cracked specimens such as [4–6] have been used widely in the literature [e.g. [7, 11, 17–22]] to obtain values of K_{mat}^ρ for notched specimens. It has recently been shown [15,16] that in most cases, such testing standards can provide reasonably accurate values of K_{mat}^ρ for notched specimens.

More recent work [23] has shown that the values of K_{mat}^ρ measured on laboratory specimens containing notches are not only dependent on the in-plane effect of the notch radius, but are also significantly affected by an out-of-plane constraint loss which is itself enhanced by the presence of the notch radius. The effect of out-of-plane constraint loss is an active research topic for sharp cracks [24,25]. For notches this out-of-plane constraint loss can have a greater effect on toughness than that of the in-plane effect of the notch radius alone. The use of experimentally measured K_{mat}^ρ values in an NFAD assessment of a notched structure may therefore be non-conservative if the out-of-plane constraint loss in the test specimen is more significant than that in the structure. The work in Ref. [23] was based solely on mechanistic modelling, and to the authors' knowledge there are no experimental data available for notched specimens to confirm the conclusions where one thickness is compared with another. The objective of the work presented in this paper is to demonstrate experimentally whether K_{mat}^ρ values for cleavage fracture are dependent on specimen thickness, and whether the effect can be successfully described using mechanistic modelling.

2. Background

The NFAD approaches in Refs. [7–12] describe the increase in effective notch toughness either as a function of ρ, or another parameter that characterises the notch radius. The approach described in Ref. [12] relates K_{mat}^{ρ} to the component of the elastic notch tip stress σ_N acting in a direction perpendicular to the plane of the notch. σ_N scales with load: a given value of σ_N could correspond to an acute notch under low load, or a blunter notch subject to a higher load. An expression for σ_N was derived by Shin [27] based on the Creager-Paris elastic stress distribution ahead of a slender notch in a uniform stress field [28]:

$$\sigma_N = \sigma\left(1 + 2Y\sqrt{\frac{a}{\rho}}\right) \quad (1)$$

where σ is the applied tensile stress remote from the notch and Y is a geometry factor used to define K_I via $K_I = Y\sigma\sqrt{\pi a}$.

The following empirical power law expression was found to describe the increase in effective cleavage toughness with increasing notch radius in Ref. [12], and preliminary work in Ref. [29] indicated that the same expression may be used to describe the increase in ductile tearing initiation toughness with notch radius:

$$\frac{K_{mat}^{\rho}}{K_{mat}} = 1 + \gamma\left[\frac{\sigma_N}{\sigma_0}\right]^{-l} \quad (2)$$

where γ and l are non-dimensional material parameters that describe the sensitivity of material toughness to the notch root radius. σ_N can be normalised using any convenient parameter, in Equation (2) it is normalised by σ_0, the yield stress defined as the stress at the limit of proportionality. Equation (2) defines the failure locus shown in Fig. 1. A loading line may be plotted on the diagram for a notched component of interest, with failure being predicted by its intersection with the failure locus. For the loading lines, the vertical axis is defined as K_J^{ρ}/K_{mat} where K_J^{ρ} is J for a notch, J^{ρ}, expressed in dimensions of K.K_J^{ρ} Can be obtained from either the J-integral, or the area under the load vs. displacement curve, using the methods described in Section 4.1. For blunt notches the loading curve rises steeply and failure is predicted at high K_{mat}^{ρ} values, and for acute notches the loading curve is less steep and failure is predicted at lower K_{mat}^{ρ} values. As $\rho \rightarrow 0$, the gradient of the failure locus at its intersection with the loading line approaches the horizontal and $K_{mat}^{\rho} \rightarrow K_{mat}$.

Depending on failure mechanism, values of γ and l that define the failure locus in Fig. 1 can be obtained using one of several methods:

(a) For initiation by cleavage and ductile tearing, curve fitting to test data plotted in the form of K_{JC}^{ρ}/K_{mat} vs. σ_N/σ_0 can be performed, where K_{JC}^{ρ} is the value of K_J^{ρ} at failure for an individual test specimen containing a notch. This is straightforward for cleavage fracture, but is less so for ductile tearing initiation due to the lack of test guidance and the practical challenges of measuring and defining tearing initiation from a notch tip.
(b) For initiation by cleavage only, the lookup table presented in Ref. [12] can be used based on a knowledge of Weibull modulus m and strain hardening exponent n.
(c) For initiation by cleavage only, a combination of (a) and (b) can be used, useful for when m is unknown but n is known.
(d) For initiation by cleavage and ductile tearing, micromechanical modelling using an appropriate local approach failure criterion can be used.

The lookup table for use in option (b) requires a knowledge of the Weibull modulus m, a parameter used in the Beremin model [30] which describes the proximity to cleavage fracture by use of the scalar Weibull stress, σ_w. In its simplest form the probability of fracture P_f is described by a two-parameter Weibull distribution:

$$P_f = 1 - \exp\left[-\left(\frac{\sigma_w}{\sigma_u}\right)^m\right] \quad (3)$$

where σ_u and m are the Weibull parameters. m is the shape parameter describing the scatter, and σ_u is the scale parameter, defined as the value of σ_w at $P_f = 0.632$. The Weibull stress is calculated by integrating a weighted value of the maximum principal stress σ_1 over the plastic zone V ahead of the stress concentration:

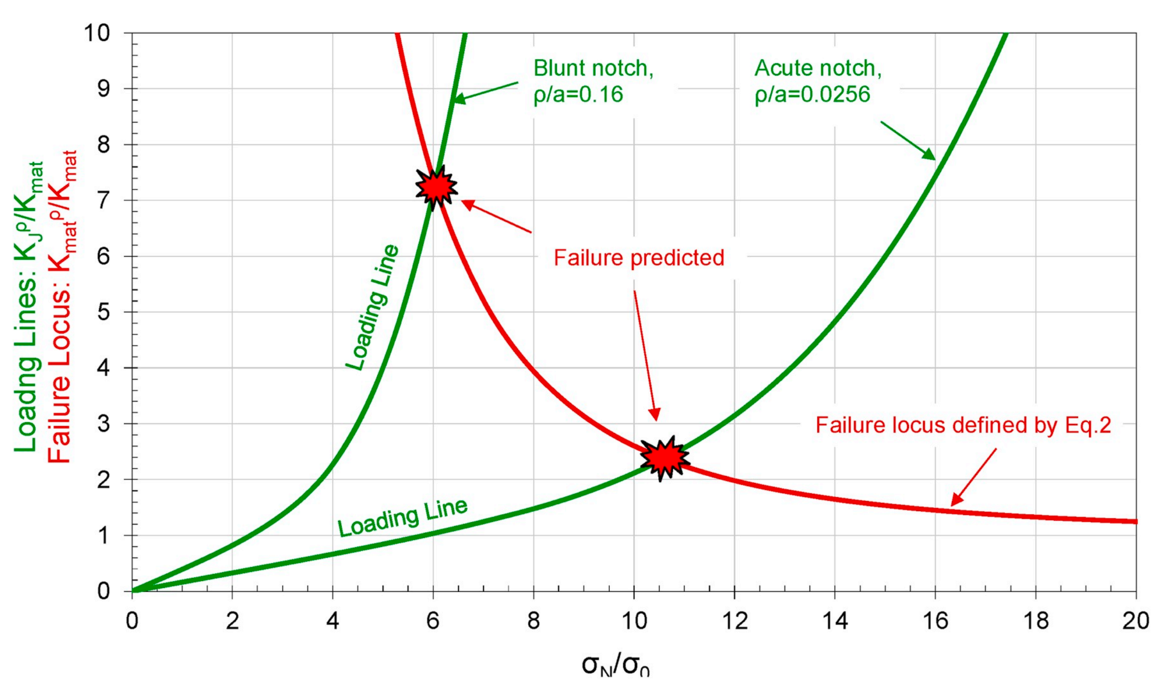

Fig. 1. Loading lines and failure locus in toughness-σ_N space.

$$\sigma_w = \left[\frac{1}{V_0}\int_V \sigma_1^m dV\right]^{1/m} \quad (4)$$

The constant V_0 is a reference volume required to ensure dimensional consistency and in the current work is taken as unity. The Weibull parameters m and σ_u are determined by matching values calculated from the Beremin model to experimental values of cleavage fracture toughness. Reliable estimation of the Weibull parameters is only possible using experimental data of sufficient quantity that cover two different constraint levels. The method proposed by Gao et al. [31] is suitable. A detailed description of the method and its application to the current work is described later in Section 4.3.1 of this paper.

One of the useful aspects of this approach, as shown in Ref. [12], is that for a given value of σ_N/σ_0, the ratio K_{mat}^{ρ}/K_{mat} remains independent of load, independent of J, independent of σ_w, and independent of cleavage fracture probability P_f. The cleavage fracture probability is introduced into the approach when a value is assigned to K_{mat}. For example, a K_{mat} value corresponding to a 5% cleavage fracture probability would enable K_{mat}^{ρ} at that same cleavage fracture probability to be defined.

3. Material

The material selected for the experimental programme was a 15 mm thick structural steel plate of grade S460 M [32] which has been used previously for studying notch effects on fracture [33,34]. Table 1 summarises the chemical composition of the material, performed by means of chemical emission spectroscopy, and Fig. 2 shows the microstructure, which comprises alternate bands of pearlite and ferrite.

The elastic modulus E was defined using the following expression due to Ingham et al. [36]:

$$E = 210000\ (MPa) - 54T \quad (5)$$

where T is the temperature in °C. The value of E at the test temperature of −100 °C was therefore taken as 215400 MPa. Poisson's ratio ν was assumed to be 0.3.

Tensile properties were measured using cylindrical tensile specimens 10 mm in diameter and machined from the centre of the plate thickness, parallel to the rolling direction (i.e. longitudinal). Four repeat tensile tests were performed at −100 °C in accordance with ASTM E8 [35]. Tensile curves were found to be discontinuous, exhibiting yield plateaus prior to strain hardening. Table 2 summarises the tensile properties σ_y (defined at 0.2% plastic strain), Ultimate Tensile Strength (UTS), and the strain at maximum load e_{max}.

Fracture toughness properties of the same plate were determined in previous work [33,34] where the Master Curve Reference Temperature, T_0 [37,38], was calculated as −91.8 °C. The fracture toughness K_{mat} as defined using the Master Curve approach includes a crack front length correction to account for the microstructural weakest link effect in pre-cracked specimens. For a given T_0, K_{mat} for any specimen thickness B, cleavage fracture probability P_f and temperature T within the transition region is defined as follows:

$$K_{mat} = 20(MPa) + \left[ln\left(\frac{1}{1-P_f}\right)\right]^{1/4}\{11 + 77exp[0.019(T - T_0)]\}\left(\frac{25}{B}\right)^{1/4} \quad (6)$$

The experimental programme focused on two specimen thicknesses, the full plate thickness of B = 15 mm, and B = 9 mm. This latter thickness was selected as the thinnest possible specimen that, if pre-cracked, would still meet the minimum thickness criterion required to ensure plane strain conditions as defined in Ref. [39]. This is discussed further in Section 6 below. For this material's T_0 value of −91.8 °C, the median fracture toughness K_{mat} at the chosen test temperature of T = -100 °C is 110.6 MPa$\sqrt{m}$ for $B = 9$ mm and 99.7 MPa$\sqrt{m}$ for $B = 15$ mm. A median fracture toughness was used for convenience for comparing with test data.

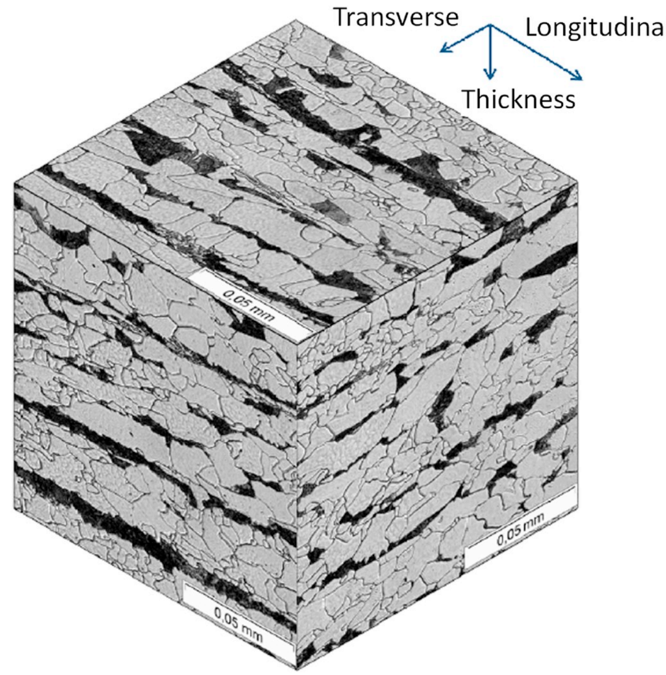

Fig. 2. Microstructure of steel S460 M, with ferritic-pearlic microstructure (sample polished and etched with Nital 2%).

Table 2
Tensile properties of steel S460 M at −100 °C.

	Test No.	σ_y (MPa)	UTS (MPa)	e_{max} (%)
S460M	1	632.0	724.5	12.0
	2	590.1	719.7	14.2
	3	622.8	722.4	11.5
	4	618.2	710.8	14.2
	Average values	615.7	719.3	12.9

4. Methodology

4.1. Experimental programme

The experimental fracture programme reported in this paper comprises 24 Single Edge Notch Bend (SENB) specimens containing notches instead of fatigue pre-cracks. This does not include the pre-cracked specimens used to determine T_0, reported in Refs. [33,34], or the notched specimens from the same papers. All specimens were machined from the same 15 mm thick plate from which the tensile specimens were machined, oriented parallel to the rolling direction, and notched in the through-thickness direction. As for the tensile tests, the fracture tests were performed at −100 °C, just below the T_0 value of −91.8 °C.

Table 1
Chemical composition of steel S460 M.

	C	Si	Mn	P	S	Cr	Mo	Ni	Al	Cu	Nb	Ti	V
S460 M	0.12	0.45	1.49	0.012	0.001	0.062	0.001	0.016	0.048	0.011	0.036	0.003	0.066

U-shaped notches were machined into the specimens using Electro-Discharge Machining (EDM) and the fracture tests were performed in accordance with ASTM E1820 [39]. In order to achieve the required test temperature, liquid nitrogen was used in combination with an insulating chamber.

The work reported in Refs. [33,34] did not consider the effect of thickness B on effective notch toughness K^{ρ}_{mat}. As the aim of the current work is to compare test results from specimens of two different thicknesses B but with all other geometrical dimensions kept the same, 24 new tests have been specifically performed for this work, with the geometrical dimensions summarised in Table 3. Six repeat tests were performed for each of the four geometries. The specimens with B = 9 mm were machined from the plate centreline. Fig. 3 shows the geometry of one type of specimen, D11-D16.

Table 3 shows that the experimental program combines two different thicknesses B (9 mm and 15 mm) and notch radii ρ (0.15 mm and 1.2 mm), but all other dimensions are kept constant. During the different tests, the applied load, the Crack Mouth Opening Displacement (CMOD) and the crosshead displacement were recorded. For some tests, the clip gauges measuring CMOD reached their maximum opening shortly before the end of the test, so in these cases CMOD for the final portion of the test was estimated. This was achieved by extrapolating the CMOD vs. time trend recorded during the mid-portion of the test. This trend was very close to being linear, but a 2nd order polynomial fit provided a more accurate fit, and this was used to extrapolate CMOD values up to the end of the test.

Load Line Displacement (LLD) was not measured in the tests, but estimates of LLD were obtained using correlations between CMOD and LLD obtained from the Finite Element (FE) models reported in the next section below. Although the relationship between CMOD and LLD in each FE model was approximately linear and approximately the same for all four geometries shown in Table 3, a second order polynomial fitted to each individual geometry provided the most accurate relationship, and these polynomial expressions were used to estimate LLD from the CMOD measured in each test.

Although the tests were performed in accordance with the ASTM procedure, ESIS P2-92 [40] was used to calculate J, denoted here as J_{ESIS}, from the area under the load vs. LLD curve using Equation (7):

$$J_{ESIS} = \frac{\eta U}{B(W-a)} \tag{7}$$

where $\eta = 2$

U = area under load vs. LLD curve.

Although Equation (7) was derived for use with pre-cracked specimens, as is the case for similar expressions in other fracture toughness testing standards, it has been shown [12,15,16,29] that such expressions provide reasonable estimates of J^{ρ}, typically to within 10% depending on notch radius and loading level. Of all these methods, J_{ESIS} generally provides the most accurate method for notched specimens, typically to within 5% [12,15].

Values of J_{ESIS} at failure were converted to dimensions of K using the following expression:

$$K^{\rho}_{JC} = \sqrt{EJ_{ESIS}/(1-\nu^2)} \tag{8}$$

To characterise the improvement in effective toughness due to the presence of the notch, it is convenient to normalise the K^{ρ}_{JC} measured for each notched specimen by the fracture toughness K_{mat}, where K_{mat} is defined for a pre-cracked specimen of the same specimen thickness B as that of the notched specimen. A different absolute value of K_{mat} is therefore used for each specimen thickness as described in Section 3 of this paper. Defined in this way, the ratio K^{ρ}_{JC}/K_{mat} compares the measured notch toughness with the equivalent fracture toughness of a pre-cracked specimen of the same thickness.

4.2. Finite Element analysis

4.2.1. SENB specimens

Three-dimensional (3D) FE models of the four SENB test specimen geometries were constructed and validated against test data. In addition to the four test specimen geometries listed in Table 3, four additional geometries were modelled corresponding to specimen thicknesses of B = 18 mm and 27 mm, corresponding to B/W ratios of 1.0 and 1.5 respectively. The complete FE model matrix is shown in Table 4. For each SENB specimen modelled, symmetry conditions were specified along the uncracked ligament (x_2=0) and the longitudinal mid-plane (x_3=B/2) thereby enabling one quarter of each SENB specimen to be modelled numerically. An example of the one-quarter model of the SENB specimen with B = 15 mm and ρ = 1.20 mm is shown in Fig. 4. Each model consisted of quadratic 20-noded reduced integration hexahedral elements (C3D20R) arranged into 14 variable thickness layers. The thickest element layer was defined at the longitudinal mid-plane with thinner elements defined near the free surface to accommodate the reduced constraint approaching plane stress conditions. Each model had a straight notch front. The FE analyses were performed using ABAQUS version 6.14-3 [41] using a finite strain formulation.

Within each of the 14 variable thickness layers, rings of elements enclosed the notch tip as shown in Fig. 5. The notch tip elements had a dimension L in the x_1 direction and a dimension approximately equal to L in the angular direction, $\theta = tan^{-1}(x_2/x_1)$. In the angular direction, 10 equally sized elements were defined in the range $0 < \theta < \pi/2$ and L was constant with θ. In the x_1 direction, L increased with increasing distance r from the centre of curvature of the notch tip, where $L = 2\pi r/40$. The ratio ρ/L was therefore the same in all models and ensured a consistency of mesh structures between the models with notches of differing radii.

The lower loading pin was modelled using a three-dimensional rigid analytical part in the shape of a cylinder positioned below the SENB specimen. Loading in three-point bending was simulated by applying a prescribed displacement in the x_2 direction to a single reference point tied to a line of nodes on the top of the specimen. This enabled the reaction force to be evaluated through the single reference point.

Plasticity was modelled using true-stress vs. true-strain data obtained from the tensile tests performed at −100 °C, and hence included the yield plateau as measured in the tensile tests. To obtain strains higher than those measured in the tensile tests, a Ramberg-Osgood relationship was used to extrapolate the test data to high strains. The stress at the limit of proportionality σ_0 was 597 MPa and the strain hardening exponent n used to extrapolate the stress-strain curve to high strains was 12.

4.2.2. Boundary layer models

The method used for calibrating the Weibull parameters, described in Section 4.3.1 below, requires the use of a plane strain boundary layer FE model to simulate a crack in an infinite body [42]. The boundary

Table 3
Test matrix with geometrical dimensions.

Codes	Description	Specimen Type	B (mm)	W (mm)	a (mm)	ρ (mm)	B/W	a/W	ρ/a
D11-D16	Thin Acute	SENB	9	18	9	0.15	0.5	0.5	0.017
D21-D26	Thin Blunt	SENB	9	18	9	1.20	0.5	0.5	0.133
E11-E16	Thick Acute	SENB	15	18	9	0.15	0.833	0.5	0.017
E21-E26	Thick Blunt	SENB	15	18	9	1.20	0.833	0.5	0.133

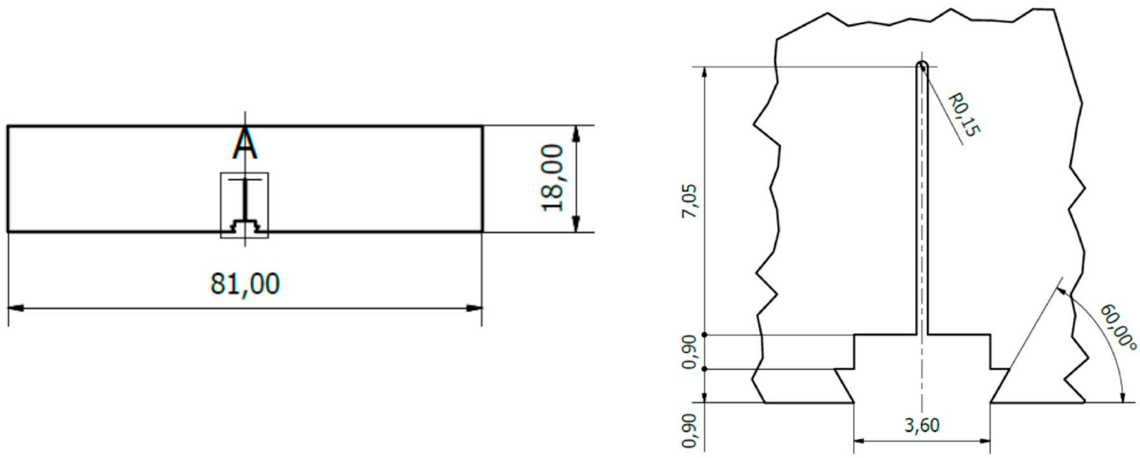

Fig. 3. SENB fracture specimens D11 to D16 (see Table 3). Dimensions in mm.

Table 4
FE matrix.

Description	Specimen Type	B (mm)	W (mm)	a (mm)	ρ (mm)	B/W	a/W	ρ/a
Geometry matched to test data.	SENB	9	18	9	0.15	0.5	0.5	0.017
	SENB	9	18	9	1.20	0.5	0.5	0.133
	SENB	15	18	9	0.15	0.833	0.5	0.017
	SENB	15	18	9	1.20	0.833	0.5	0.133
No corresponding test data. Geometry modelled to investigate behaviour at higher thicknesses.	SENB	18	18	9	0.15	1.0	0.5	0.017
	SENB	18	18	9	1.20	1.0	0.5	0.133
	SENB	27	18	9	0.15	1.5	0.5	0.017
	SENB	27	18	9	1.20	1.5	0.5	0.133

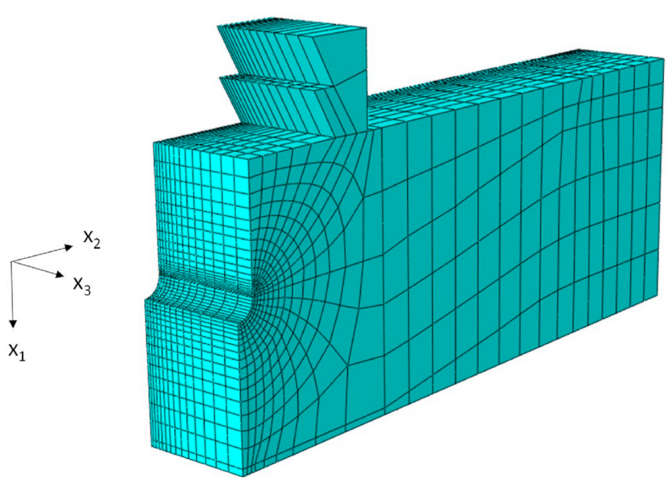

Fig. 4. One-quarter FE model of SENB specimen E21-E26 (B = 15 mm, ρ = 1.20 mm).

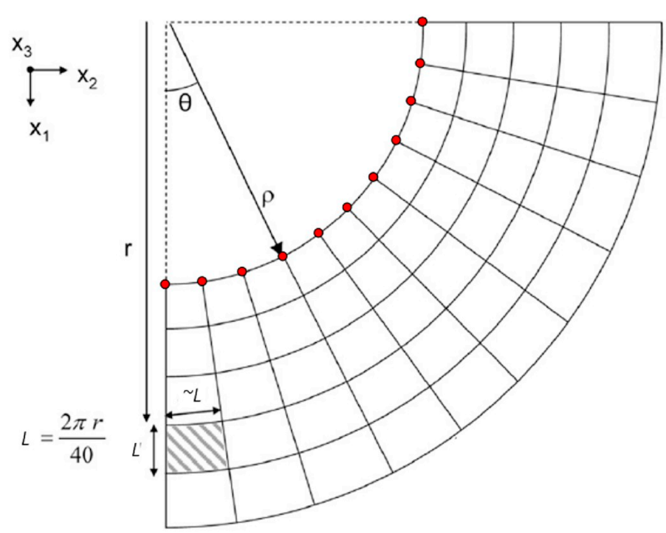

Fig. 5. Notch tip mesh detail.

layer model consisted of a semi-circular mesh of initial radius R containing a radial crack modelled with a crack tip radius $\rho = 2.5$ μm. The ratio R/ρ was set at 10^5 to ensure that the crack tip plastic zone did not approach the boundary of the model thereby ensuring small-scale yielding conditions were preserved. Symmetry conditions were specified along the uncracked ligament (x_2=0). Plane strain boundary conditions were applied to both faces in the x_3 direction, so the model was essentially 2D despite the same 3D elements being used as for the SENB specimens, i.e. quadratic 20-noded reduced integration elements. Although the boundary layer model is essentially a plane strain analysis, the thickness of the model affects the volume of the crack tip plastic zone and hence the Weibull stress as defined by Equation (4). Four boundary layer models were analysed, each model having a thickness equal to that of each SENB model.

Displacement boundary conditions were applied incrementally to the nodes on the outer edge of the model. These displacements were consistent with the leading, K_I-dominated term of the Williams expansion [43] for the displacement field at the crack tip, as follows:

$$u_1 = K_I \frac{1+\nu}{E} \sqrt{\frac{R}{2\pi}} \cos\left(\frac{\theta}{2}\right)(3-4\nu-\cos\theta) \tag{9}$$

$$u_2 = K_I \frac{1+\nu}{E}\sqrt{\frac{R}{2\pi}}\sin\left(\frac{\theta}{2}\right)(3-4\nu-\cos\theta) \tag{10}$$

where u_1 and u_2 are the displacements in the x_1 and x_2 directions respectively, E is the elastic modulus, ν is Poisson's ratio, and the polar co-ordinates R and θ define the position of the node with respect to the crack tip. Plasticity was modelled using the same stress-strain relationship used for the SENB models.

4.3. Post-processing

4.3.1. Calibration of weibull parameter, m

The approach proposed by Gao et al. [31] provides a suitable methodology for determining m and σ_u and can be summarised in the following steps:

1. Test two sets of fracture toughness specimens, one set corresponding to high constraint conditions (geometry A) and the other to low constraint conditions (geometry B).
2. Perform 3D elastic-plastic FE analyses of both specimen geometries tested (A and B). The models should have sufficient mesh refinement to allow accurate calculation of the Weibull stress σ_w and the crack driving force J.
3. Perform 2D plane strain elastic-plastic FE analysis of a defect in an infinite body under SSY conditions using a boundary layer model.
4. Calibrate m as follows:
   a. Assume an m value (or several trial values of m) and calculate the σ_w vs. J history for the A and B specimen geometries and for the SSY analysis
   b. Constraint correct each measured J value from the A and B specimen geometries to its equivalent SSY equivalent value. This is defined as the value of J under small scale yielding which has the same scalar Weibull stress (and therefore failure probability) as the measured values of J.
   c. Calculate two estimates of the SSY scale factor for the two distributions of constraint-corrected J values. For N toughness values, a simple estimate is given by:

$$\xi^{A,B} = \left[\frac{1}{N}\left(\sum_{i=1}^{N} J^2_{(i)-SSY}\right)\right]^{1/2} \tag{11}$$

   d. Repeat steps (a-c) with different values of m until $\xi^A = \xi^B$ within a small tolerance, thereby minimising the error function $R(m) = (\xi^A - \xi^B)/\xi^B$.
5. For the calibrated value of m, the value of σ_u is the value of σ_w in the boundary layer model corresponding to a crack driving force of $\xi^A = \xi^B$.

The above method has previously been implemented for SENB specimens containing notches in Ref. [26] where it was noted that care is required during calibration to ensure that the constraint states of the high constraint geometry A and the low constraint geometry B span the defect of interest. This ensures that the model interpolates between the constraint states used for calibration, rather than extrapolating outside the range of applicability. For this reason, for Step 1, the thick specimen with an acute notch (E11-E16 in Table 3) was selected as the high constraint geometry A, and the thin specimen with a blunt notch (D21-D26) as the low constraint geometry B. This was to ensure the scaling model is applicable over the widest range of constraint states.

The calibration approach adopted uses SENB specimens of two different thicknesses, and for this reason Step 3 involved boundary layer analysis of the same two thicknesses as the SENB test specimens used for calibration. The constraint correction procedure in Step 4b therefore corrected each specimen geometry to the equivalent SSY value for the boundary layer model of the same thickness, as shown schematically in Fig. 6. In Step 5, one value of σ_u was obtained for each thickness.

Equation (3) describes the probability of cleavage initiation only and does not account for subsequent micro-crack arrest (i.e. it assumes that cleavage initiation corresponds to macroscopic cleavage fracture). The two-parameter Weibull distribution therefore tends to over-predict the observed scatter in fracture toughness test results. This limitation led to an alternative expression being proposed [44] based on a three-parameter distribution:

$$P_f = 1 - \exp\left[-\left(\frac{\sigma_w - \sigma_{w,min}}{\sigma_u - \sigma_{w,min}}\right)^m\right] \tag{12}$$

where $\sigma_{w,min}$ is the minimum value of Weibull stress at which macro-

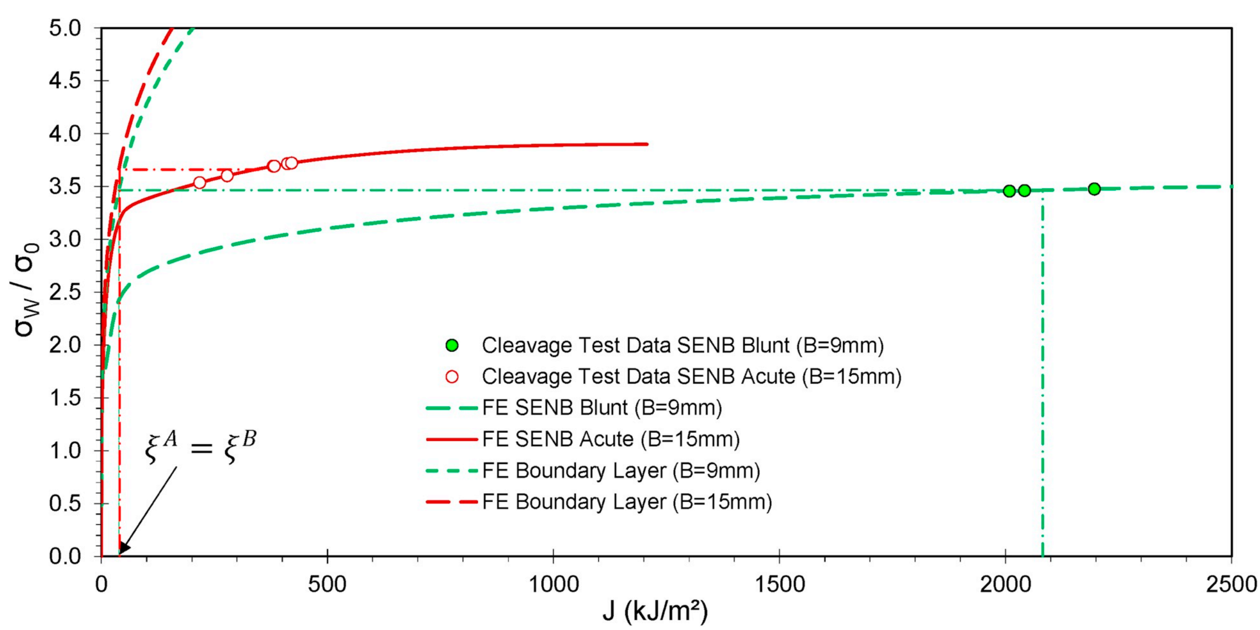

Fig. 6. Toughness scaling diagram.

scopic cleavage fracture becomes possible. $\sigma_{w,min}$ is conventionally defined as the σ_w value in SSY that corresponds to the lowest possible K_J value at fracture, K_{min}, of 20 MPa$\sqrt{m}$ as specified in ASTM E1921 [38]. For specimens with notches instead of fatigue pre-cracks, experimental data from steel specimens tested at very low temperatures (for example at −196 °C in Ref. [18]) indicate that even on the lower shelf, the measured effective notch toughness is significantly higher than the fracture toughness, which suggests that K_{min} may be larger than 20 MPa/m for specimens with notches. In this work, values of $\sigma_{w,min}$ corresponding to a higher value of K_{min}, arbitrarily set at 50 MPa$\sqrt{m}$, were considered in addition to the standard value of 20 MPa$\sqrt{m}$ quoted for pre-cracked specimens in ASTM E1921.

4.3.2. Weibull stress based toughness scaling model

The toughness scaling model based on the Weibull stress [45] was originally developed for constraint correction between cracked specimens of differing constraint levels with different levels of applied J but identical cleavage fracture probabilities. The same approach was first applied to specimens containing cracks and notches of differing root radius in Ref. [26], and a similar approach has been adopted in this work.

Toughness scaling diagrams, such as those shown in Fig. 6, were generated by post-processing numerical data (maximum principal stresses and integration point volumes) from each FE model to define the evolution of σ_w, calculated using Equation (4), with the value of J. For the SENB specimens, J_{ESIS} was calculated according to ESIS P2-92 using Equation (7), for consistency with the analysis of the test data. For the boundary layer models representing SSY, J cannot be obtained from Equation (7) so J was instead obtained using contour independent J-integrals.

The probability of cleavage fracture is directly related to the Weibull stress via Equation (3). For specimens of the same thickness and therefore the same value for σ_u, a horizontal line plotted in Fig. 6 defines a specific cleavage fracture probability. Fig. 6 can then be used to predict the value of J that corresponds to a given failure probability for any other geometry modelled of the same thickness. For specimens of different thickness and hence different values of σ_u, the toughness scaling model approach can still be used, but it is more convenient to plot P_f instead of σ_w on the ordinate axis to account for the different value of σ_u for each specimen thickness.

5. Results

5.1. Experimental data

Fig. 7 plots the experimentally measured load vs. LLD curves for the SENB specimens together with the corresponding curves from the FE analyses. The FE analyses are discussed later in the paper. Most of the specimens failed in a brittle manner during a rising load. Examination of the fracture surfaces indicated failure occurred predominantly by cleavage fracture without significant ductile tearing, depicted by the circles in Fig. 7. As an example, the fracture surface for specimen D26 is shown in Fig. 8; despite extensive plastic deformation being apparent near the free surface, no significant pre-cleavage ductile tearing was visible on the fracture surface. In contrast, some of the other thinner specimens with $B/W = 0.5$ did not fail by cleavage before maximum load was reached, and for these specimens the point of maximum load is represented by squares in Fig. 7. For two specimens, problems during the test led to the test being stopped before fracture or maximum load was reached, these are shown by diamonds in Fig. 7.

From Fig. 7 it is evident that the thicker specimens exhibited much higher loads than the thinner specimens, as would be expected due to the larger cross sectional area and hence greater load bearing capacity, and they also exhibited lower displacement values at failure than the thinner specimens. In terms of fracture mechanics, it is more useful to discuss the results in terms of the measured effective toughness, and this was calculated from the area under load vs. displacement curve using J_{ESIS} (Equation (7)) and converting to K^{ρ}_{JC} (Equation (8)). These values are summarised in Table 5 which tabulates the failure type, load at failure, and the values of J_{ESIS} and K^{ρ}_{JC} at failure.

Fig. 9(a) presents the experimental results in terms of K^{ρ}_{JC} plotted against B/W. K_{mat} values obtained using the Master Curve (Equation (6)) for pre-cracked specimens are also plotted for comparison, with the points corresponding to the median value and the error bars denoting the 5th and 95th percentile values of K_{mat}. Fig. 9(a) clearly shows a significant reduction in toughness with increasing specimen thickness for both acute and blunt notches. These data provide clear experimental evidence of the thickness effect that occurs in steel specimens with notches. Fig. 9(b) presents the same results as Fig. 9(a) but plotted in the same form as Fig. 1 with K^{ρ}_{JC}/K_{mat} on the ordinate axis and σ_N/σ_0 on the abscissa axis, where σ_N is calculated using Equation. (1). As the thickness of the pre-cracked specimen used to define K_{mat} is equal to that of the notched specimen, the thickness effect in Fig. 9(b) can be attributed to the differences in the extents of out-of-plane constraint loss between the two specimens.

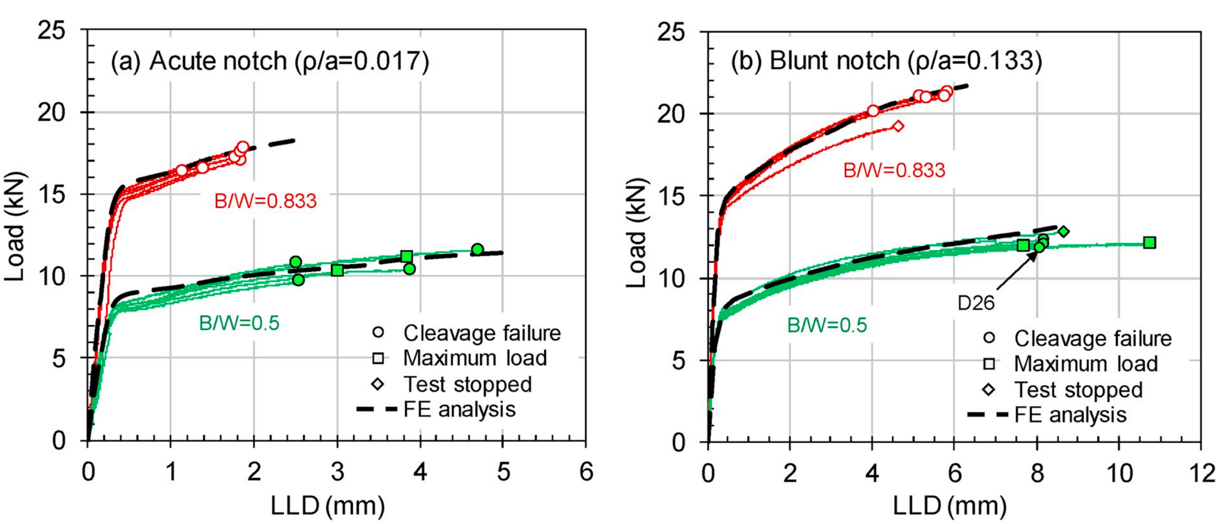

Fig. 7. Load vs. displacement curves from the experimental programme showing specimens with (a) an acute notch and (b) a blunt notch.

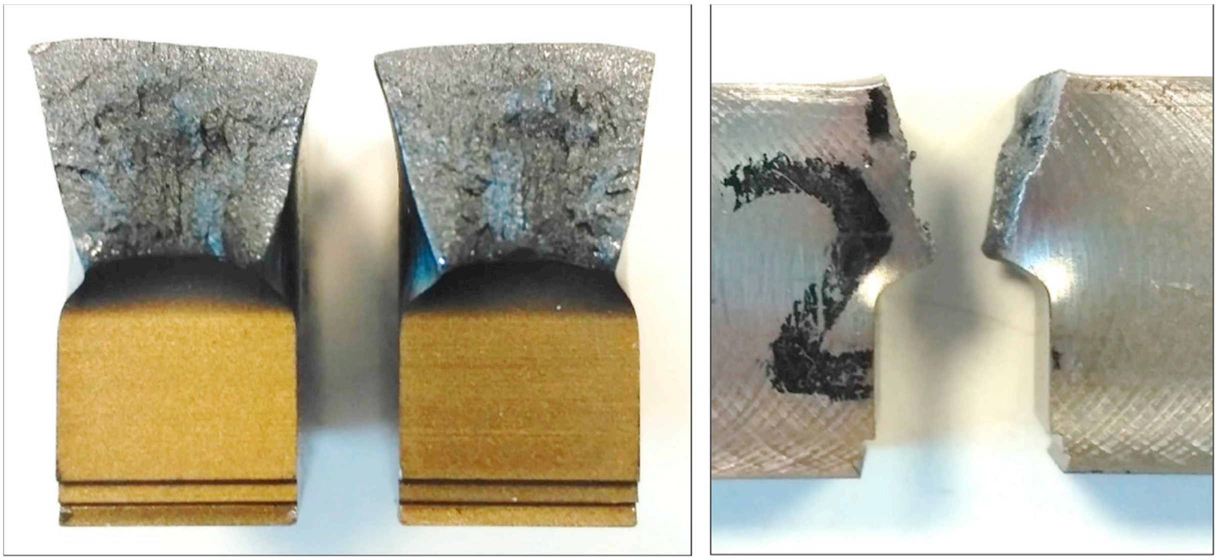

Fig. 8. Fracture surface for specimen D26 showing extensive plastic deformation at the free surface but no visible ductile tearing preceding cleavage fracture.

Table 5
Experimental results.

Specimen ID	B (mm)	W (mm)	a (mm)	ρ (mm)	B/W	ρ/a	Failure		J_{ESIS} (kJ/m^2)	K^{ρ}_{JC}(MPa$\sqrt{m}$)
							Type	Load (kN)		
D11	9	18	9	0.15	0.5	0.017	Cleavage	10.80	561	364.2
D12	9	18	9	0.15	0.5	0.017	Cleavage	11.55	1146	520.7
D13	9	18	9	0.15	0.5	0.017	Max Load	11.13	898	461.1
D14	9	18	9	0.15	0.5	0.017	Cleavage	10.38	859	450.9
D15	9	18	9	0.15	0.5	0.017	Max Load	10.24	658	394.7
D16	9	18	9	0.15	0.5	0.017	Cleavage	9.65	506	346.0
D21	9	18	9	1.20	0.5	0.133	Stopped	12.84	2322	741.3
D22	9	18	9	1.20	0.5	0.133	Cleavage	12.29	2196	721.0
D23	9	18	9	1.20	0.5	0.133	Cleavage	12.08	2042	695.3
D24	9	18	9	1.20	0.5	0.133	Max Load	12.10	2852	821.6
D25	9	18	9	1.20	0.5	0.133	Max Load	11.90	1968	682.6
D26	9	18	9	1.20	0.5	0.133	Cleavage	11.85	2009	689.5
E11	15	18	9	0.15	0.833	0.017	Cleavage	17.04	380	299.8
E12	15	18	9	0.15	0.833	0.017	Cleavage	17.23	382	300.8
E13	15	18	9	0.15	0.833	0.017	Cleavage	17.56	412	312.1
E14	15	18	9	0.15	0.833	0.017	Cleavage	16.31	217	226.7
E15	15	18	9	0.15	0.833	0.017	Cleavage	17.76	421	315.6
E16	15	18	9	0.15	0.833	0.017	Cleavage	16.49	278	256.6
E21	15	18	9	1.20	0.833	0.133	Stopped	19.26	1135	518.3
E22	15	18	9	1.20	0.833	0.133	Cleavage	21.24	1565	608.6
E23	15	18	9	1.20	0.833	0.133	Cleavage	20.11	1032	494.2
E24	15	18	9	1.20	0.833	0.133	Cleavage	21.02	1361	567.6
E25	15	18	9	1.20	0.833	0.133	Cleavage	21.03	1528	601.4
E26	15	18	9	1.20	0.833	0.133	Cleavage	20.96	1417	579.1

Curves have also been fitted to the test data in Fig. 9(b) using Equation (2). These are best-fit curves through the middle of the test data, so the normalising toughness K_{mat} has also been defined at the median level. If curves were fitted as a lower-bound, for example through the lower 5th percentile of the test data, then the normalising toughness K_{mat} would also be defined at the lower 5th percentile for consistency. Although the individual K^{ρ}_{JC}/K_{mat} data points would be higher in this case, the fitted K^{ρ}_{mat}/K_{mat} curve would be unchanged. As discussed in Section 2, this is one of the useful aspects of the approach: for a given value of σ_N/σ_0, the ratio K^{ρ}_{mat}/K_{mat} remains independent of load, independent of J, independent of σ_w, and independent of cleavage fracture probability P_f. However, the same P_f must be used for the definition of both K^{ρ}_{mat} and K_{mat} for consistency.

5.2. *Finite Element analysis*

Fig. 7 compares the load vs. LLD output from the FE analyses with the test data. The FE results correlate well with the test data, with the FE results lying within the scatter of the test data. For the acute notch with $\rho/a = 0.017$, the FE results slightly over-predict the load at the yield point. A reduction in accuracy of FE models around the yield point has been observed previously [46] for acute notches when modelling materials that exhibit discontinuous yielding with stress-strain curves that retain the Lüders band. The over-prediction of load at the yield point is relatively small in the current case, and as fracture of the test specimens occurs well beyond yield, this is not expected to have a significant impact on the modelling results at failure.

5.2.1. *Calibration of weibull parameter, m*

As discussed earlier, the thick SENB with acute notch was selected as

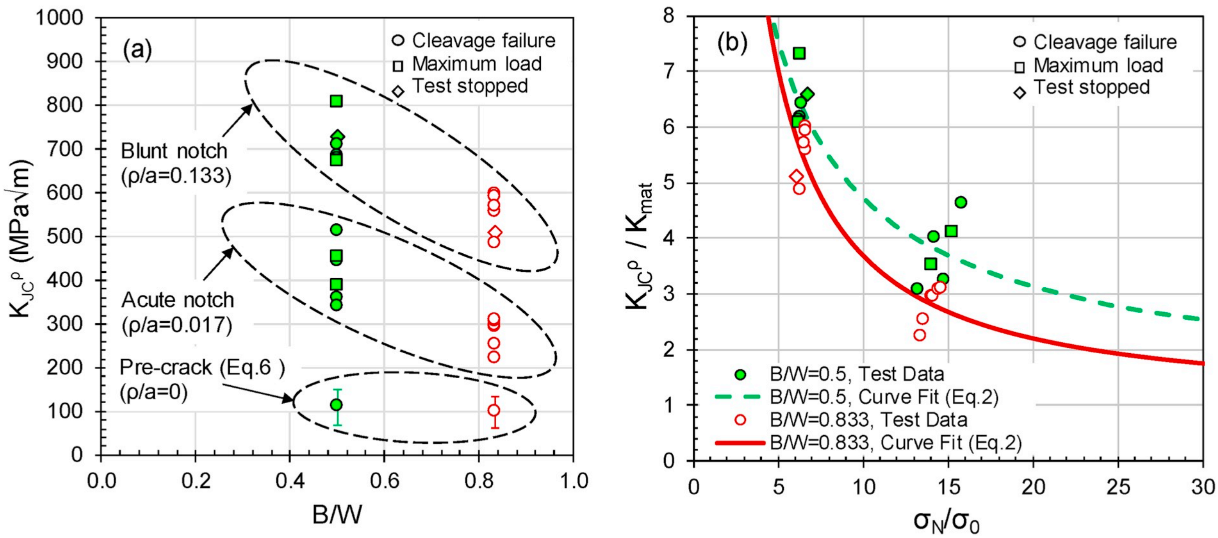

Fig. 9. Experimentally measured K_{JC}^{ρ} values plotted (a) against specimen thickness B,(b) normalised in the form K_{JC}^{ρ}/K_{mat} vs. σ_N/σ_0.

the high constraint geometry A. All six of these specimens failed by cleavage without prior ductile tearing and are therefore suitable to use for calibration. The thin SENB with blunt notch was selected as the low constraint geometry B, but unfortunately only three of these specimens failed by cleavage without prior ductile tearing. Calibration of the Weibull parameters ideally requires larger datasets – typically ten repeats at each condition – so the size of the available datasets is much smaller than would be preferred. Despite the small calibration datasets, an attempt was made to calibrate the parameters.

To calibrate the Weibull modulus m, initial trial values of $m = 10,11,12,\ldots,19$ were chosen. A plot of the error function $R(m)$ vs. m indicated a zero value for the function would be achieved with m slightly below 10. A second iteration of steps 4a-4c from Section 4.3.1 of the paper was therefore carried out for m = 9.0,9.1,9.2,…,9.9. A plot of $R(m)$ vs. m showed the error function was close to zero at m = 9.1. This was taken to be the 'calibrated' value of m. Applying step 5 of the procedure resulted in different values of σ_u/σ_0 for each specimen thickness modelled, and these values are summarised in Table 6.

5.2.2. Failure predictions

Fig. 10 compares the predicted values of P_f, calculated using Equation (12), with the values of σ_w/σ_0 at failure. Predictions for the thinner specimens with $B/W = 0.5$ are shown in Fig. 10(a) and those for the thicker specimens with $B/W = 0.833$ are shown in Fig. 10(b). The Weibull stress model tends to over-predict the scatter when using the standard K_{min} value of 20 MPa$\sqrt{}$m specified for pre-cracked specimens in ASTM E1921. The use of a higher K_{min} value reduces the spread of the predictions and brings them into closer alignment with the test data, however the use of a higher value also raises the question of the most appropriate value to select for K_{min} when assessing notched specimens (the value of 50 MPa$\sqrt{}$m is an arbitrarily selected value to show the sensitivity of the approach to this value). It is therefore convenient to consider the results at $P_f = 0.632$, where the predictions are insensitive to the value assumed for K_{min} and hence insensitive to $\sigma_{w,min}$.

The datasets used for calibration are shown as solid black circles, so

Table 6
Calibrated Weibull parameters for different thicknesses.

B/W	m	σ_u/σ_0
0.5	9.1	3.47
0.833		3.67
1.0		3.74
1.5		3.91

the predictive capability of the method can be judged by comparing the prediction with the open circles. The predictions for the thin specimens match very well with the acute notch test data Fig. 10(a), however for the thicker specimens the model under-predicts failure of the blunt notch specimens Fig. 10(b). Given the relatively small datasets used for calibration of m, the close correlation between predictions and test data for the thin specimens in Fig. 10(a) is perhaps more surprising than the under-prediction of the blunt specimen in Fig. 10(b).

Fig. 11(a) compares the predicted values of K_{JC}^{ρ} with the test data, plotted against B/W. K_{mat} values obtained using the Master Curve (Equation (6)) for pre-cracked specimens are also plotted for comparison at $P_f = 0.632$. The predictions, which were made at the two discrete B/W values of 0.5 and 0.833, have been joined together with straight black lines for the purposes of clarity, although in reality the trend is unlikely to be linear. The predictions would be expected to pass close to the centre of the experimental data; although they are reasonable for the thinner specimens, there is a tendency to under-predict K_{JC}^{ρ} for the thicker, blunter notch, which is consistent with Fig. 10(b). This same trend is also noticeable in Fig. 11(b), which shows the same test results and predictions but plotted in a form consistent with Fig. 1. Despite this under-prediction, the overall general trend of the variation of K_{JC}^{ρ} with B/W appears broadly reasonable considering the reduction in accuracy expected due to the limited data that was available for calibration.

5.2.3. Toughness scaling to other thicknesses

Toughness scaling predictions for SENB specimens with thicknesses greater than those in the experimental programme are presented in Fig. 12. The toughness scaling diagram for the blunt notch radius with ρ/a = 0.133 is shown in Fig. 12(a), plotted in terms of P_f on the ordinate axis calculated using Equation (12) with $K_{min} = 20$ MPa$\sqrt{}$m, and J on the abscissa axis calculated using Equation (7). Predicted values of effective notch toughness are plotted in Fig. 12(b) as a function of B/W, where the predictions correspond to $P_f = 0.632$ for consistency with the results presented in Fig. 11(a). The FE predictions indicate that for both notch radii, the effective notch toughness becomes relatively insensitive to thickness above $B/W = 0.833$. The test data are in agreement for the acute notch, but as the FE under-predicts K_{JC}^{ρ} for the blunt notch, it could be argued that the insensitive region starts closer to $B/W = 1.0$.

6. Discussion

The effect of thickness on effective notch toughness has previously been discussed in Ref. [47]. The magnitude of the effect was predicted

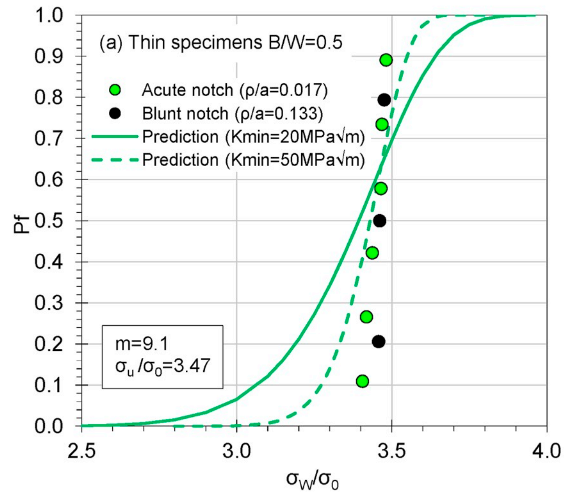

Fig. 10. Failure predictions for (a) thin specimens with B/W = 0.5,(b) thick specimens with B/W = 0.833.

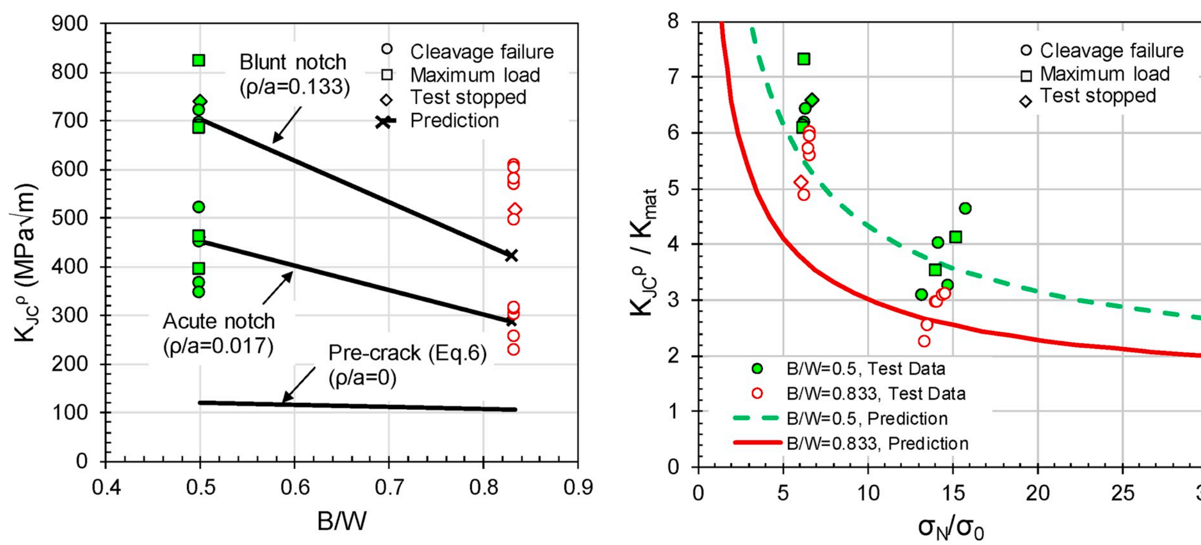

Fig. 11. Failure predictions (a) plotted against $\boldsymbol{B/W}$,(b) normalised in the form $\boldsymbol{K_{JC}^{\rho}/K_{mat}}$ vs. $\boldsymbol{\sigma_N/\sigma_0}$

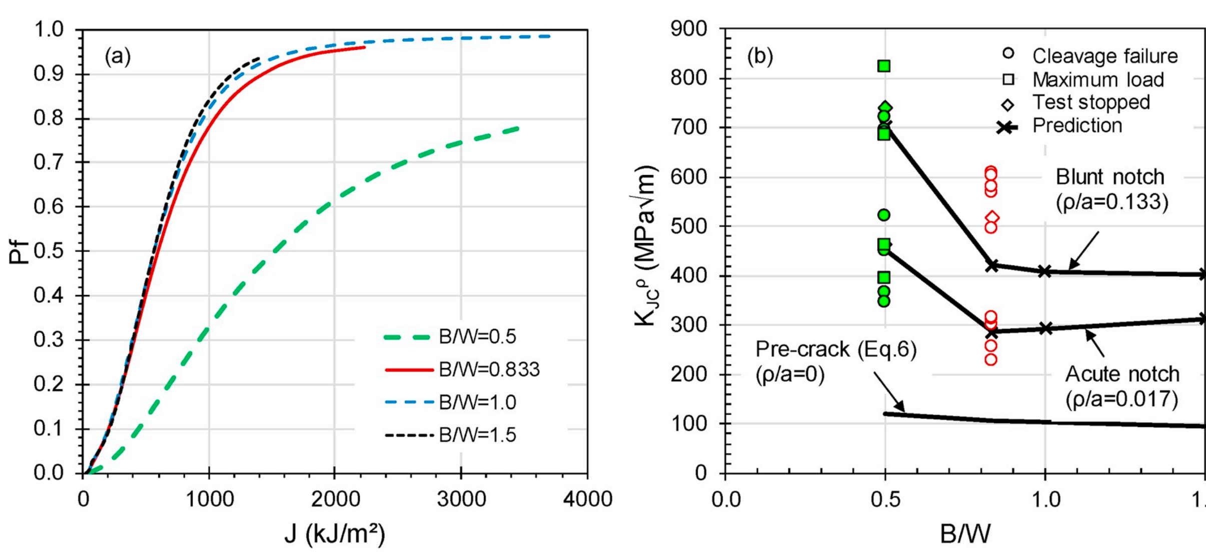

Fig. 12. FE predictions for thicknesses up to $\boldsymbol{B/W} = 1.5$, (a) toughness scaling diagram for $\boldsymbol{\rho/a} = 0.133$, (b) predictions for both notch radii plotted against.$\boldsymbol{B/W}$

using Weibull stress analysis in Ref. [23], and the test data in this paper provide clear experimental evidence of this effect.

When values of K_{JC}^{ρ} are plotted without being normalised by K_{mat}, such as in Figs. 9(a) and Figure 11(a), the observed thickness effect is due to a combination of two distinct components: primarily a mechanical out-of-plane constraint loss effect due to the loss of plane strain conditions that occurs with decreasing thickness; and to a lesser degree a microstructural weakest link effect which is relevant for cleavage fracture. The latter effect arises due a shorter crack front length and hence smaller plastic zone volume decreasing the probability of sampling a microstructural feature capable of triggering cleavage fracture, compared with a thick specimen. Normalising the values of K_{JC}^{ρ} by the corresponding fracture toughness K_{mat} for a pre-cracked specimen of the same thickness, e.g. Figs. 9(b) and Figure 11(b), results in plots that show only the mechanical constraint loss effect.

The overall toughness benefit defined by K_{mat}^{ρ}/K_{mat} therefore arises due to a combination of the in-plane effect of the notch radius and the out-of-plane constraint loss which itself is enhanced by the presence of the notch radius. Both the test data and the FE predictions indicate that for the thin SENB specimens with $B/W = 0.5$, the out-of-plane constraint loss is as significant as the in-plane effect of the notch radius alone. This is consistent with the numerical study of Compact Tension (CT) specimens in Ref. [23] which showed the out-of-plane constraint loss effect was as significant as the in-plane notch effect for CT specimens with $B/W = 0.5$.

Fracture toughness testing standards such as [38,39] provide minimum thickness requirements to ensure that the out-of-plane constraint loss is minimised in pre-cracked test specimens, for example [39]:

$$B \geq \frac{100J}{\sigma_y} \tag{13}$$

where J is defined for a pre-cracked specimen. Equation (13) was used to design the test programme in this paper, specifically to select the thinnest possible specimen that would still meet this criterion if the specimen was pre-cracked instead of notched. Using the Master Curve to define median fracture toughness properties, Equations (6) and (13) were solved for a range of trial thickness values to find the lowest integer value of B that would satisfy Equation (13), and hence meet the standard criterion to ensure plane strain conditions for a pre-cracked specimen. This resulted in $B = 9$ mm (i.e. $B/W = 0.5$) being chosen for the thinnest specimen in the test programme. In contrast, for the test specimens containing notches, the results in Fig. 12(b) indicate that a minimum thickness closer to $B/W = 1.0$ is required to minimise out-of-plane constraint loss. This finding is consistent with the numerical analysis in Ref. [23] which showed that although significant out-of-plane constraint loss occurred in CT specimens with $B/W = 0.5$, doubling the thickness to $B/W = 1.0$ was sufficient to eliminate the out-of-plane constraint loss. It is important to note that halving the width W instead of doubling the thickness B to achieve the same ratio $B/W = 1.0$ would not achieve the same result; not only would the specimen still be affected by out-of-plane constraint loss, but the reduced W may also lead to in-plane constraint loss. It is therefore important to note that a specific B/W ratio should not be regarded as a universal criterion for eliminating out-of-plane constraint loss, the ratio has used in this paper only as a convenient normalised measure of specimen thickness. Any universal criterion for defining the minimum specimen thickness to ensure plane strain conditions would be in the form of a modification to Equation (13), rather than a single B/W ratio.

The philosophy adopted in BS7910 [2] is to measure fracture toughness using full thickness test specimens, i.e. specimens with a thickness B equal to the thickness of the structure being assessed. Although this is appropriate for assessing cracked structures using pre-cracked test specimens which meet the minimum thickness requirements, test specimens containing notches are more likely to suffer from out-of-plane constraint loss than pre-cracked specimens of the same thickness. Therefore, even full-thickness test specimens may exhibit higher toughness than would be expected if conditions were fully plane strain. Using such a value of K_{mat}^{ρ} would be non-conservative in an NFAD assessment if the non-sharp defect in the structure being assessed was in plane strain, for example the deepest part of a long surface-breaking notch.

7. Conclusions

The main conclusions of this work are as follows:

- The test data in this paper provide clear experimental evidence of a significant thickness effect on the effective cleavage toughness K_{mat}^{ρ} measured using SENB specimens containing a U-notch instead of a pre-crack. This effect is over and above the microstructural weakest link effect arising from differences in the volume of the plastic zone.
- The toughness benefit due to the notch, K_{mat}^{ρ} / K_{mat}, is a function of both the in-plane effect of the notch radius and an out-of-plane constraint loss which itself is enhanced by the presence of the notch radius. The test data and FE modelling results indicate that the effect of this out-of-plane constraint loss on K_{mat}^{ρ} / K_{mat} can be of the same order of magnitude as the in-plane effect of the notch radius alone.
- For the material considered in this paper, significant out-of-plane constraint loss occurred for notched specimens with $B/W = 0.5$, a geometry that if pre-cracked would have met the minimum thickness requirement mandated by ASTM E1820.
- Doubling the thickness to $B/W = 1.0$ was sufficient to eliminate the out-of-plane constraint loss for the material and geometry considered, an observation consistent with a previous numerical study [23]. K_{mat}^{ρ} was relatively insensitive to thickness for $B/W>1.0$.
- The use of experimentally measured K_{mat}^{ρ} values in an NFAD assessment of a structure may be non-conservative if $B/W<1.0$, due to the loss of plane strain conditions in the test specimen.

CRediT authorship contribution statement

A.J. Horn: Conceptualization, Methodology, Software, Formal analysis, Investigation, Resources, Writing - original draft, Visualization, Project administration, Funding acquisition. **S. Cicero:** Conceptualization, Methodology, Formal analysis, Investigation, Resources, Writing - original draft, Visualization, Supervision, Project administration, Funding acquisition. **D. Andrés:** Investigation, Writing - review & editing.

Acknowledgements

This paper is published with the permission of Wood, the University of Cantabria, and the UK Atomic Energy Authority. The authors of this work would like to express their gratitude for financial support from:

• The Spanish Ministry of Science and Innovation, under project MAT2014-58443-P: "Análisis del comportamiento en fractura de componentes estructurales con defectos en condiciones debajo confinamiento tensional", on which the results of this paper are based;

• Wood, via a contribution to the R6 Development Programme;

• The Research Councils UK (RCUK) Energy Programme [grant number EP/P012450/1]. To obtain further information on the data and models underlying this paper please contact: PublicationsManager@ukaea.ac.uk.

References

[1] R6 – Revision 4: Assessment of the Integrity of Structures Containing Defects, Amendment 11, EDF Energy, Gloucester, UK, March 2015.

[2] BSI. BS7910:2013+A1:2015, Incorporating Corrigenda Nos. 1 and 2, 2016: Guide on Methods for Assessing the Integrity of Flaws in Metallic Structures, British Standards Institution, 2016.
[3] API 579-1/ASME FFS-1, Fitness-for-Service, jointly published by the, American Petroleum Institute and the American Society for Mechanical Engineers, June 2016.
[4] BSI. BS 7448-1, Fracture Mechanics Toughness Tests - Part 1: Method for Determination of KIC, Critical CTOD and Critical J Values of Metallic Materials, British Standards Institution, 1999.
[5] ASTM E1820-11, Standard Test Method for Measurement of Fracture Toughness, ASTM, 2011.
[6] ESIS. ESIS P2-92, ESIS Procedure for Determining the Fracture Behaviour of Materials, 1992.
[7] W.Q. Wang, A.J. Li, P.N. Li, D.Y. Ju, Engineering approach for notch elastic-plastic fracture analysis, Int. J. Press. Vessel. Pip. 60 (1994) 1–16.
[8] E. Smith, Fracture initiation at the root of a blunt flaw: description in terms of Kr-Lr failure assessment curves, Int. J. Press. Vessel. Pip. 76 (11) (1999) 799–800.
[9] Y.G. Matvienko, Local fracture criterion to describe failure assessment diagrams for a body with a crack/notch, Int. J. Fract. 124 (2003) 107–112.
[10] S. Cicero, F. Gutierrez-Solana, A.J. Horn, Experimental analysis of differences in mechanical behaviour of cracked and notched specimens in a ferritic-pearlitic steel: considerations about the notch effect on structural integrity, Eng. Fail. Anal. 16 (2009) 2450–2466.
[11] S. Cicero, F. Gutiérrez-Solana, J.A. Álvarez, Structural integrity assessment of components subjected to low constraint conditions, Eng. Fract. Mech. 75 (10) (2008) 3038–3059.
[12] A.J. Horn, A.H. Sherry, An engineering assessment methodology for non-sharp defects in steel structures - Part I: procedure development, Int. J. Press. Vessel. Pip. 89 (2012) 137–150.
[13] J.-J. Han, N.O. Larossa, Y.-J. Kim, R.A. Ainsworth, Blunt defect assessment in the framework of the failure assessment diagram, Int. J. Press. Vessel. Pip. 146 (2016) 39–54.
[14] A.J. Horn, C. Aird, Limits of applicability of the notch failure assessment diagram, in: Proceedings of the ASME 2018 Pressure Vessels and Piping Conference, July 15-20, 2018. Prague, Czech Republic. PVP2018-85062.
[15] A.J. Horn, P.J. Budden, Development of test guidance for single edge notch bend fracture toughness specimens containing notches instead of fatigue pre-cracks, in: Proceedings of the ASME 2015 Pressure Vessels and Piping Conference, July 19-23, 2015. Boston, Massachusetts, USA. PVP2015-45474.
[16] A.J. Horn, P.J. Budden, Development of test guidance for compact tension fracture toughness specimens containing notches instead of fatigue pre-cracks, in: Proceedings of the 23rd Conference on Structural Mechanics in Reactor Technology (SMiRT-23), Manchester, UK, August 10-14, 2015. Paper no. 287.
[17] S. Cicero, T. Garcia, V. Madrazo, J. Cuervo, E. Ruiz, F. Gutierrez-Solana, Analysing the notch effect within the ductile-to-brittle transition zone of S275JR steel, in: Proceedings of the ASME 2013 Pressure Vessels and Piping Conference, July 14-18, 2013. Paris, France. PVP2013-97017.
[18] S. Cicero, V. Madrazo, T. Garcia, J. Cuervo, E. Ruiz, On the notch effect in load bearing capacity, apparent fracture toughness and fracture mechanisms of polymer PMMA, aluminium alloy Al7075-t651 and structural steels S275JR and S355J2, Eng. Fail. Anal. 29 (2013) 108–121.
[19] S. Cicero, F. Gutierrez-Solana, J.A. Alvarez, Structural integrity assessment of components subjected to low constraint conditions, Eng. Fract. Mech. 75 (2008) 3038–3059.
[20] J.D. Landes, J.A. Begley, Experimental methods for elastic-plastic and post-yield fracture toughness measurements, in: D.G.H. Latzko (Ed.), Post-yield Fracture Mechanics, Applied Science Publishers Ltd, London, 1979, pp. 211–253.
[21] P. Livieri, Use of J-integral to predict static failures in sharp V-notches and rounded U-notches, Eng. Fract. Mech. 75 (2008) 1779–1793.
[22] E. Barati, F. Berto, Fracture assessment of U-notches under mode I loading by means of critical value of the J-integral, Procedia Eng. 10 (2011) 807–812.
[23] A.J. Horn, A.H. Sherry, P.J. Budden, Size and geometry effects in notched compact tension specimens, Int. J. Press. Vessel. Pip. 154 (2017) 29–40.
[24] Y.G. Matvienko, The effect of out-of-plane constraint in terms of the T-stress in connection with specimen thickness, Theor. Appl. Fract. Mech. 80 (2015) 49–56.
[25] Z. Liu, X. Wang, J. Tang, C. Deng, H. Zhao, X. Chen, The effects of in-plane and out-of-plane constraints on J-R curves for X80 steel: a study using clamped SENT specimens, Eng. Fract. Mech. 206 (2019) 342–358.
[26] A.J. Horn, A.H. Sherry, Prediction of cleavage fracture from non-sharp defects using the Weibull stress based toughness scaling model, Int. J. Press. Vessel. Pip. 87 (2010) 670–680.
[27] C.S. Shin, A discussion on various estimations of elastic stress distributions and stress concentration factors for sharp edge notches, Int. J. Fatigue 8 (4) (1986) 235–237.
[28] M. Creager, P.C. Paris, Elastic field equations for blunt cracks with reference to stress corrosion cracking, Int. J. Fract. Mech. 3 (1967) 247–252.
[29] J.S. Kim, N.O. Larrosa, A.J. Horn, Y.J. Kim, R.A. Ainsworth, Notch bluntness effects on fracture toughness of a modified S690 steel at 150°C, Eng. Fract. Mech. 188 (2018) 250–267.
[30] F.M. Beremin, A local criterion for cleavage fracture of a nuclear pressure vessel steel, Metall. Trans. A 14A (1983) 2277–2287.
[31] X. Gao, C. Ruggieri, R.H. Dodds Jr., Calibration of Weibull stress parameters using fracture toughness data, Int. J. Fract. 92 (2) (1998) 175–200.
[32] EN 10025-4:2004, Technical Delivery Conditions for Thermomechanical Rolled Weldable Fine Grain Structural Steels, European Committee for Standardization, 2004.
[33] S. Cicero, T. García, V. Madrazo, Application and validation of the Notch Master Curve in medium and high strength structural steels, J. Mech. Sci. Technol. 29 (2015) 4129–4142.
[34] S. Cicero, T. García, V. Madrazo, Structural integrity analysis of notched ferritic steels operating within their ductile-to-brittle transition zone: an approach from Failure Assessment Diagrams and the Notch Master Curve, Eng. Fail. Anal. 58 (2015) 134–148.
[35] ASTM E8-E8M-13a, Standard Test Methods for Tension Testing of Metallic Materials, American Society for Testing and Materials, Philadelphia, USA, 2013.
[36] T. Ingham, N. Knee, I. Milne, E. Morland, Fracture toughness in the transition regime for A533B-1 steel: prediction of large specimen results from specimen tests, ASTM STP 1020 (1989) 369–389.
[37] K. Wallin, The size effect in K_{Ic} results, Eng. Fract. Mech. 22 (1985) 149–163.
[38] ASTM E1921-13a, Test Method for the Determination of Reference Temperature T0 for Ferritic Steels in the Transition Range, American Society for Testing and Materials, Philadelphia, USA, 2013.
[39] ASTM E1820-13, Standard Test Method for Measurement of Fracture Toughness, American Society for Testing and Materials, Philadelphia, 2013.
[40] ESIS P2-92, ESIS Procedure for Determining the Fracture Behaviour of Materials, ESIS, 1992.
[41] ABAQUS 6.12. ABAQUS Documentation, Dassault Systemes, Providence, (RI, USA).
[42] B.A. Bilby, G.E. Cardew, M.R. Goldthorpe, I.C. Howard, A finite element investigation of the effect of specimen geometry on the fields of stress and strain at the tips of stationary cracks, in: Size Effects in Fracture, Mechanical Engineering Publications, 1986, pp. 37–46.
[43] M.L. Williams, Stress singularities resulting from various boundary conditions in angular corners of plates in extension, J. Appl. Mech. 19 (1952) 526–528.
[44] X. Gao, C. Ruggieri, R.H. Dodds Jr., Calibration of Weibull stress parameters using fracture toughness data, Int. J. Fract. 92 (2) (1998) 175–200.
[45] C. Ruggieri, R.H. Dodds Jr., A transferability model for brittle fracture including constraint and ductile tearing effects: a probabilistic approach, Int. J. Fract. 79 (1996) 309–340.
[46] A.J. Horn, S. Cicero, A. Bannister, P. Budden, Development of guidance for the assessment of non-sharp defects using the notch failure assessment diagram, in: Proceedings of the ASME 2016 Pressure Vessels and Piping Conference, July 17-21, 2016. Vancouver, British Columbia, Canada. PVP2016-63537.
[47] D. Taylor, The Theory of Critical Distances: a New Perspective in Fracture Mechanics, Elsevier, Oxford, UK, 2007.